



**HAL**  
open science

## Active damping of 'parasitic' vibration modes of a quartz sensor

Yann Meyer, Manuel Collet

► **To cite this version:**

Yann Meyer, Manuel Collet. Active damping of 'parasitic' vibration modes of a quartz sensor. *Smart Materials and Structures*, 2008, 17 (6), pp.065006. 10.1088/0964-1726/17/6/065006 . hal-00347768

**HAL Id: hal-00347768**

**<https://hal.science/hal-00347768>**

Submitted on 3 May 2023

**HAL** is a multi-disciplinary open access archive for the deposit and dissemination of scientific research documents, whether they are published or not. The documents may come from teaching and research institutions in France or abroad, or from public or private research centers.

L'archive ouverte pluridisciplinaire **HAL**, est destinée au dépôt et à la diffusion de documents scientifiques de niveau recherche, publiés ou non, émanant des établissements d'enseignement et de recherche français ou étrangers, des laboratoires publics ou privés.



Distributed under a Creative Commons Attribution - NonCommercial 4.0 International License

# Active damping of ‘parasitic’ vibration modes of a quartz sensor

Y Meyer<sup>1</sup> and M Collet<sup>2</sup>

<sup>1</sup> Institut Supérieur de Mécanique de Paris (SUPMECA Paris), LISMMA/Structures,  
3, rue Fernand Hainaut, 93407 Saint Ouen Cedex, France

<sup>2</sup> FEMTO ST département LMARC, UMR 6174, 25 000 Besançon, France

An original control approach for active vibration stabilization of sensors made of quartz is introduced in this paper. The idea explored is to use the piezoelectric framework of sensors, with respect to their operation, so as to damp ‘parasitic’ vibration modes. To accomplish this, actuating electrodes are conveniently located on the device surface by means of a simple optimization approach. The proposed stabilization control is implemented and optimized for a monolithic vibrating inertial sensor made of quartz. The performance and the energy cost of modeling are compared with the experimental ones.

## 1. Introduction

Many sensing components are made of piezoelectric materials [1–3]. For precise sensing applications, the two key properties are high quality factor and good temperature stability. Compared to other piezoelectric materials, a quartz crystal provides an interesting combination of properties. The material properties of quartz are highly repeatable, manufacturable and extremely stable with respect to temperature shifts and ageing. The frequency–temperature coefficient can be limited by a precise crystal cut (AT-cut, BT-cut, SC-cut . . .) [4–6]. Intrinsically, quartz structures have limited changes of material properties over a given period of time [7]. For example, the common ageing rate for commercial quartz resonators is approximately 5 ppm (parts per million) per year. Moreover, the internal losses of quartz material are very low [8], so that an intrinsic quality factor of about  $10^7$  at 1 MHz can be easily obtained. For these singular properties, quartz is largely and commonly used for sensing applications [9, 10] in many scientific fields [11].

Good operation of sensing electronic components, such as inertial sensors [12], is essential to the operation of electronic cards used in various civil and military applications. Sensitive components endure intense accelerations due to vibrations of their host structure. Their frequency stability, measurement accuracy and service life are strongly disturbed by these vibrations, and the improvement of dynamics of sensors is

currently a major economic and strategic issue. One of the best ways to improve a vibratory behavior is to use an active control process [13]. Generally, this solution is applied to the host electronic cards by using piezoelectric patches [14–17]. Another solution is to control the vibratory behavior of electronic components themselves. Limiting the vibration transfer between an element and its support can be one method [18–20]. Another method is to modify the parameters of the studied structure (for example, stiffness) with environmental shifts. This original method is examined in the paper. The principal idea is to individually stabilize each sensitive component made of quartz, by using the piezoelectric properties of their framework. The simplest way is to design a multi-electrode set-up deposited onto a quartz framework in order to actively control it. The main benefit of this strategy is the smallness of the amount of mass to be controlled. In this case, the required control energy level remains moderate and can be provided by electrical energy sources, already implemented on the host electronic cards. Thus, the electrode network necessary to the stabilization process has to be integrated into the design phase of sensitive components.

The control law is founded on a classical collocated sky-hook strategy with an absolute sensor [13, 21]. An actuator and a sensor are considered as collocated whenever they are physically at the same spot on the structure and energetically dual. Due to the dimensional specifications of the studied sensors (from a few millimeters to micrometers), the

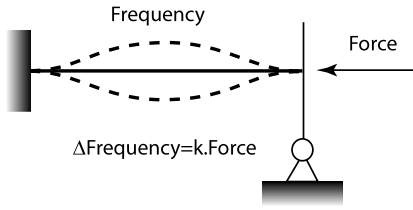


**Figure 1.** Force–frequency effect on a vibrating beam.

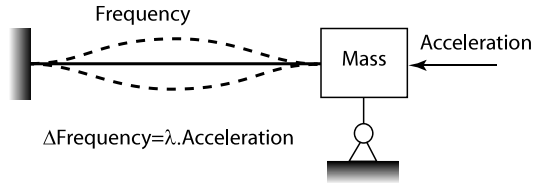


**Figure 2.** Force–frequency effect on a vibrating beam through a proof-mass.

transducing elements can be considered as pseudo-collocated. Alternation of poles and zeros of the transfer function associated with the system guarantees the control loop stability. In this case, sky-hook vibration control is the simplest and the most common control strategy. This method is robust and unconditionally stable [13]. The idea is to actively introduce, in a mechanical framework, a viscous damper rigidly fixed to a stationary coordinate system. The design of this controller is based on an absolute sensing signal such as acceleration, transmitted force, absolute velocity or absolute displacement. Studies of various sky-hook-type strategies are broadly proposed in the literature [22].

The objective of this study is to design, manufacture and test a multi-actuating electrode set-up integrated onto a sensor framework in order to prove active stabilization feasibility for an single sensitive component by using its piezoelectric substrate.

The paper is organized as follows. Section 2 describes operation of a monolithic vibrating inertial sensor, made of quartz, and operation of the studied structure. In section 3, a piezoelectric linear formulation, applied to quartz material, is provided. This section is a base for the numerical development of the optimization criterion in section 4. In the following section, the topological optimization process is performed for the studied accelerometer. Optimization constraints are given to clearly set the validity domain of the following control strategy. The efficiency and the energy cost of numerical control strategy are compared with experimental ones, in section 6. Finally, conclusions are discussed.

## 2. Monolithic vibrating inertial sensors

### 2.1. Operation of a monolithic vibrating inertial sensor

Monolithic vibrating inertial sensors, made of quartz crystal, constitute an innovating research field. The principle of physics used in vibrating sensors is the force–frequency effect [23, 24]. As shown in figure 1, this effect is based on the

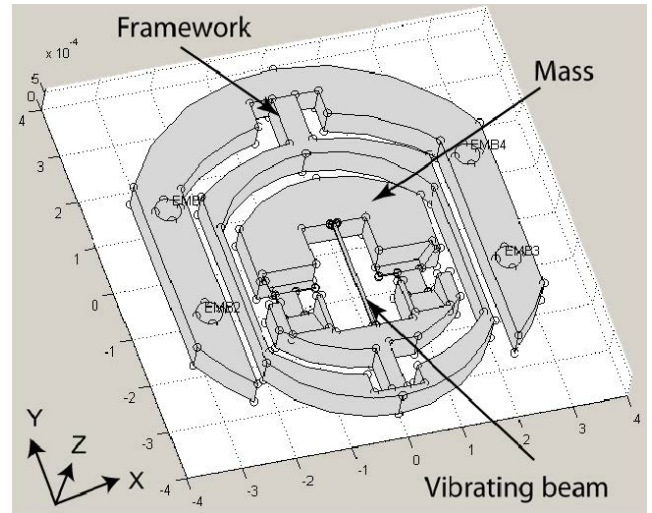


**Figure 3.** Computer-aided design modeling of a monolithic vibrating accelerometer.

resonance-frequency shift of a bending structure subjected to an external tensile or compressive stress. Resonance-frequency variation is very close to being proportional to the amplitude of input stresses [24].

The design basis of a monolithic sensing element is the use of micro-machining collective methods, such as the chemical etching process. Thus, several products are machined in a one-time process [25]. So, it becomes simpler and cheaper to produce and miniaturize new generations of inertial sensors. The most common applications are vibrating gyrometers [26–28], vibrating beam force sensors [29–31] and vibrating beam accelerometers [32, 33, 35, 36]. In the paper, the device that we consider is a monolithic vibrating accelerometer made of quartz crystal.

### 2.2. Operation of a monolithic vibrating accelerometer

The principle of a monolithic vibrating accelerometer is quite simple. A cantilever with a tip mass is considered. This bending beam, made of quartz, is excited in its first natural frequency by the piezoelectric effect. Acceleration acts on the mass and then forces this beam in tension or in compression as shown in figure 2. Small amplitudes of motion are assumed for the proof-mass. Rotational effects are neglected. Thus, the result is a variation of the first natural frequency proportional to acceleration.

The technological device is given in the literature [34–36]. The whole structure is made of quartz crystal. The typical dimensions of this device are  $8 \times 10^{-3}$  m diameter and  $5 \times 10^{-4}$  m thick. In figure 3, a computer-aided design modeling of a monolithic vibrating accelerometer is presented.

The vibrating beam is excited on its first natural frequency, about 65 kHz. The sensor is aimed at detecting frequency shift due to acceleration applied to the proof-mass along the sensitive axis ( $\vec{Y}$ -axis). The sensor framework keeps the mass in a stable position at rest and concentrates the maximal useful vibrating energy in the middle of the device. Moreover, this framework is designed to uncouple the sensitive axis and

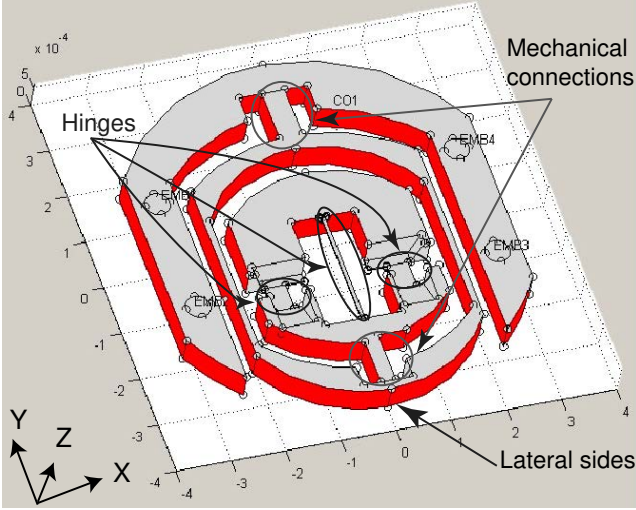


**Figure 4.** Different mechanical connections of a monolithic vibrating accelerometer. The red parts of the device are called the lateral sides.

others. Mechanical connections of the framework and hinges between the proof-mass and the framework are very stiff along the sensitive  $\vec{Y}$ -axis and more flexible along the other axes. The different connections are presented in figure 4.

An ideal case is considered. The three axes are assumed to be perfectly uncoupled and the first natural frequency of the structure is preponderant along each axis. Only the sensitive axis and the  $\vec{Z}$ -axis are considered for simplicity. A modal projection provides one one-degree-of-freedom system, that is to say an equivalent ‘mass–spring–damper’ system, for each axis.

The eigenfrequency of the structure along the sensitive axis is far above the operating point of the beam because of the high stiffness of the mechanical connection along this axis. The eigenfrequency of the structure along the  $\vec{Z}$ -axis is far below the operating point of the beam because of the low bending stiffness of the mechanical connection along this axis. Consequently, excitations along the  $\vec{Z}$ -axis are filtered at the operating point, as shown in figure 5.

Unfortunately, the case presented in figure 5 is without imperfections. In reality, the different axes are coupled by inevitable micro-machining imperfections. The natural modes of the structure along the axis  $\vec{X}$  and  $\vec{Z}$  also constrain the central beam. Thus, they disturb good operation of the sensor along its sensitive axis. Indeed, when signal processing is performed to extract acceleration, the presence of these parasitic resonances affects the process and degrades measurement precision. Consequently, it becomes necessary to control these inevitable ‘parasitic’ vibration modes to minimize this drawback.

### 3. Piezoelectric linear formulation

#### 3.1. Governing equations

In a structural domain  $\Omega_0$ , mechanical displacement  $\mathbf{u}$  and electric potential  $V$  satisfy stress equations of motion (Navier’s

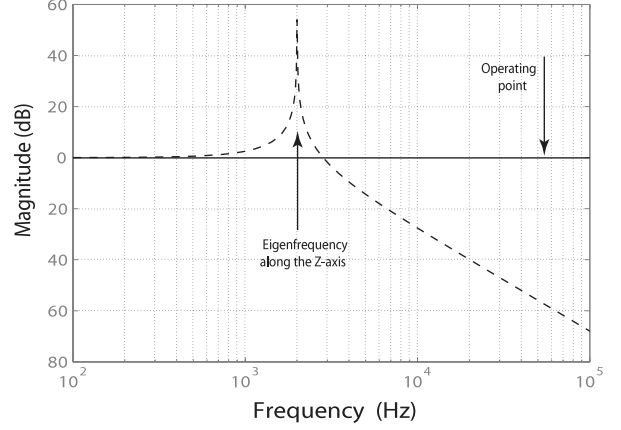


**Figure 5.** Schematic transfer functions between external acceleration, applied to the device base, and acceleration endured by the mass along the  $Y$ -axis (solid line) and the  $Z$ -axis (dotted line) in log-scale and for a random excitation.

equation) and Gauss’s law of electrostatics.

$$\sigma_{ij,i} + \mathbf{f}_j = \rho \ddot{\mathbf{u}}_j \quad (1)$$

$$\mathbf{D}_{i,i} = \rho_e = 0 \quad (2)$$

where  $\sigma$  represents the mechanical stress tensor ( $\text{N m}^{-2}$ ),  $\mathbf{D}$  electric displacement ( $\text{C m}^{-2}$ ),  $\rho$  mass density ( $\text{kg m}^{-3}$ ),  $\rho_e$  volume charge density ( $\text{C m}^{-3}$ ) and  $\mathbf{f}$  external volume force density ( $\text{N m}^{-3}$ ).

Associated mechanical boundary conditions are

$$\begin{aligned} \mathbf{u} &= \mathbf{u}_0 & \forall x \in \partial\Omega_0^u \\ \mathbf{n}_i \sigma_{ij} &= \bar{\mathbf{t}}_j & \forall x \in \partial\Omega_0^T \end{aligned} \quad (3)$$

where  $\partial\Omega_0^u$  and  $\partial\Omega_0^T$  represent respectively Dirichlet mechanical conditions and Neumann mechanical conditions and  $\mathbf{n}$  an outward normal vector at  $\partial\Omega_0^T$ .

Associated electric boundary conditions

$$\begin{aligned} V &= 0 & \forall x \in \partial\Omega_0^V \\ V &= V_a & \forall x \in \partial\Omega_a^V \\ [\mathbf{n}_i \mathbf{D}_i] &= 0 & \forall x \in \partial\Omega_0^q \end{aligned} \quad (4)$$

where  $\partial\Omega_0^V$ ,  $\partial\Omega_a^V$  and  $\partial\Omega_0^q$  represent respectively Dirichlet electrical conditions, Dirichlet electrical conditions at input/output electrical surfaces and Neumann electrical conditions, and  $\mathbf{n}$  an outward normal vector at  $\partial\Omega_0^q$ .

#### 3.2. Quartz crystal constitutive equations

In order to determine the solution of the piezoelectric vibration problem, we will have to know the arrays of material coefficients for the particular symmetry of quartz crystal. Because of their symmetry, mechanical stress and strain tensors can be brought together in stress  $\mathbf{T}$  and strain  $\mathbf{S}$  vectors containing six independent values by using the compressed matrix notation (IEEE standard).

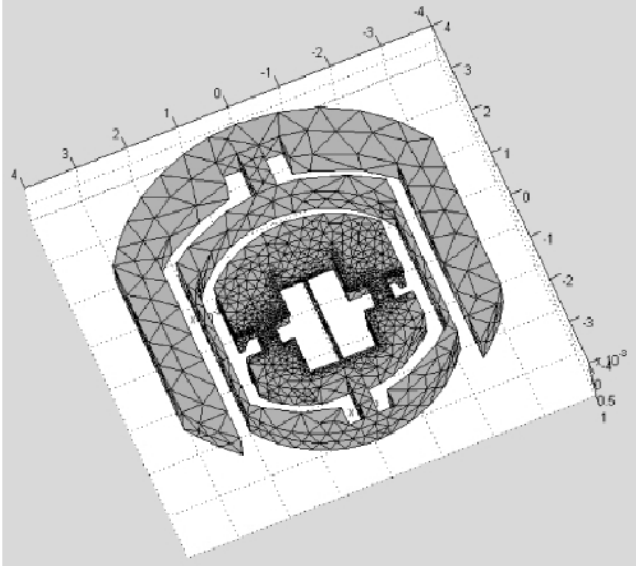


Figure 6. Meshed structure.

The piezoelectric behavior law can be described by tensor relations. These equations express the main constitutive formulations between stress and strain tensors. If the magnetic and thermal effects are considered negligible, multiphysics relationships are written in compressed matrix notation as follows:

$$\mathbf{T}_p = c_{pq}^E \mathbf{S}_q - e_{kp} \mathbf{E}_k \quad (5)$$

$$\mathbf{D}_i = e_{iq} \mathbf{S}_q + \varepsilon_{ik}^S \mathbf{E}_k \quad (6)$$

where  $\mathbf{E} = -\nabla V$ .

$c^E$ ,  $\varepsilon^S$ ,  $e$  and  $\mathbf{E}$  are respectively the elasticity matrix at constant electric field ( $\text{N m}^{-2}$ ), dielectric permittivity matrix at constant strain ( $\text{F m}^{-1}$ ), quartz electromechanical coupling matrix ( $\text{C m}^{-2}$ ) and electric field vector ( $\text{V m}^{-1}$ ). The coefficients of matrices (7), (8) and (9) are extracted from [37]. The mass density of the quartz crystal is  $2648 \text{ kg m}^{-3}$ .

$$e_{kp} = \begin{bmatrix} e_{11} & -e_{11} & 0 & e_{14} & 0 & 0 \\ 0 & 0 & 0 & 0 & -e_{14} & -e_{11} \\ 0 & 0 & 0 & 0 & 0 & 0 \end{bmatrix} \quad (7)$$

where  $e_{11} = 0.171$  and  $e_{14} = -0.046$ .

$$c_{pq}^E [10^{10}] = \begin{bmatrix} c_{11} & c_{12} & c_{13} & c_{14} & 0 & 0 \\ c_{12} & c_{11} & c_{13} & -c_{14} & 0 & 0 \\ c_{13} & c_{13} & c_{33} & 0 & 0 & 0 \\ c_{14} & -c_{14} & 0 & c_{44} & 0 & 0 \\ 0 & 0 & 0 & 0 & c_{44} & c_{14} \\ 0 & 0 & 0 & 0 & c_{14} & \frac{c_{11}-c_{12}}{2} \end{bmatrix} \quad (8)$$

where  $c_{11} = 8.67$ ,  $c_{12} = 0.7$ ,  $c_{13} = 1.19$ ,  $c_{14} = -1.79$ ,  $c_{33} = 10.72$  and  $c_{44} = 5.79$ .

$$\varepsilon_{ik}^S [10^{-11}] = \begin{bmatrix} \varepsilon_{11} & 0 & 0 \\ 0 & \varepsilon_{11} & 0 \\ 0 & 0 & \varepsilon_{33} \end{bmatrix} \quad (9)$$

where  $\varepsilon_{11} = 3.91$  and  $\varepsilon_{33} = 4.1$ .

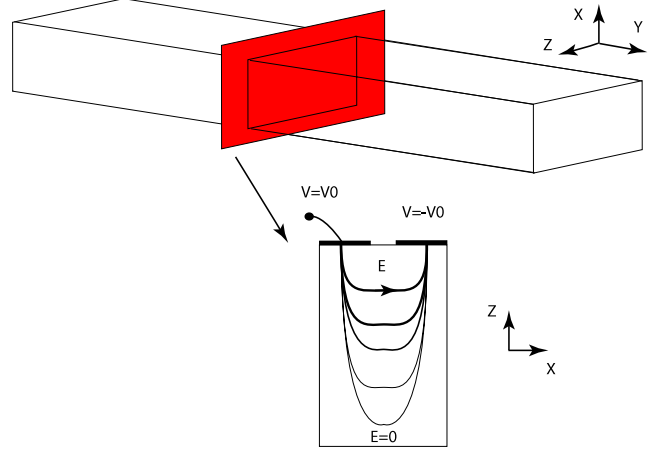


Figure 7. Evolution of the second principal strain on the top surface of the device for the studied parasitic mode.

Rotations, defining crystal cut, have to be applied to the electromechanical coupling matrix, permittivity matrix and elasticity matrix, as defined in relationships (10). An easy way to perform these rotations is the use of a Bond matrix [38]. A Bond matrix,  $M$ , is a matrix composed of the classical rotation matrix,  $a$ , but each quadrant of the Bond matrix is different combinations of the classical rotation matrix.

$$\begin{aligned} e^* &= aeM^T \\ c^{E*} &= Mc^E M^T \\ \varepsilon^{S*} &= a\varepsilon^S a^T. \end{aligned} \quad (10)$$

## 4. Optimization criterion

In this section, we seek an optimization criterion taking into account the structural parameters of the device and acting on the shape of the actuating electrodes. Due to design constraints, an appropriate choice of electrode shape has been retained.

### 4.1. Design constraints and electrode shape

Due to the sensor geometry, actuating electrodes cannot be deposited on the lateral sides. Moreover, one of the faces is reserved for the operating electrodes of the sensor. Thus, actuating electrodes are deposited only onto one surface of the device. The minimal gap between the electrodes is limited by the metallization process to  $5 \times 10^{-6} \text{ m}$ . Paschen's law [39] specifies the breakdown voltage for a chosen gap. It is about  $550 \text{ V}$  in a primary vacuum of  $10^{-2} \text{ mbar}$ .

### 4.2. Optimization criterion

In equation (5), we consider the displacement vector  $\mathbf{u}$  as a harmonic function of time,  $t$ , with a pulsation  $\omega$  ( $\text{rad s}^{-1}$ ). The subscripts are dropped from the different functions for simplicity. By introduction of (5) into (1), we obtain the weak

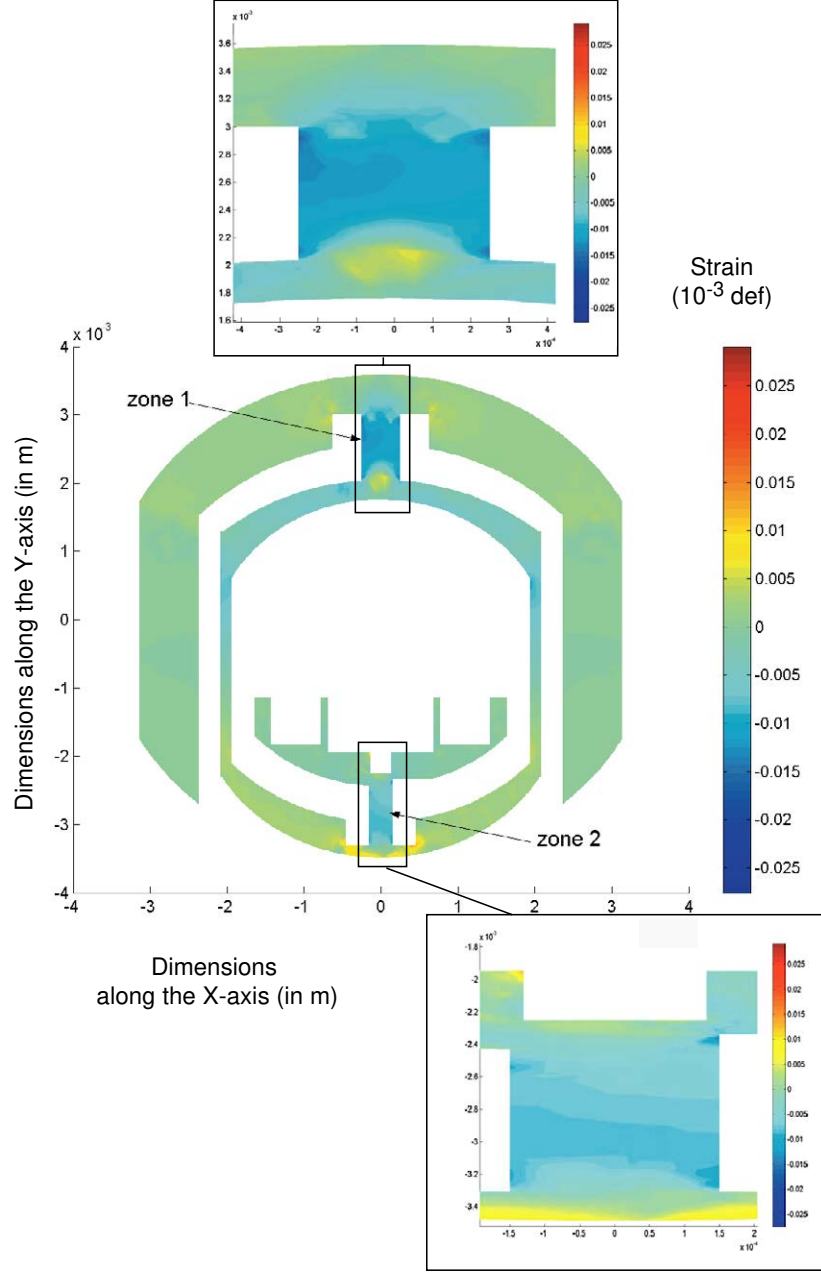


**Figure 8.** Evolution of the electric field along the thickness axis in electrostatics for the used quartz crystal.

formulation (11) for the actuation part. Note that \* indicates the tensor is rotated with respect to the crystal cut angles.

$\forall \tilde{\mathbf{u}}$  an admissible displacement field,

$$\begin{aligned}
 \int_{\Omega_0} \tilde{\mathbf{u}} \cdot (\nabla \mathbf{T} - \mathbf{f} - \rho \omega^2 \mathbf{u}) \, d\Omega_0 &= 0 \\
 \Leftrightarrow \int_{\partial \Omega_0^T} \tilde{\mathbf{u}} \cdot \tilde{\mathbf{t}} \, d\partial \Omega - \int_{\Omega_0} (\tilde{\mathbf{S}} \cdot (c^{E*} \mathbf{S}) + \tilde{\mathbf{u}} \cdot (\mathbf{f} + \rho \omega^2 \mathbf{u})) \, d\Omega_0 \\
 &= \underbrace{\int_{\Omega_0} \tilde{\mathbf{S}} \cdot (e^{T*} \mathbf{E}) \, d\Omega_0}_C
 \end{aligned}$$

where  $\tilde{\mathbf{t}}_j$  is defined in equation (3).

The energy term  $C$  proves that, in order to inject the maximum of a ‘control energy’ in the structure by the piezoelectric effect, it is necessary to design actuating electrodes so as to maximize electric field on the areas of maximum strain for the studied modes. Thus, the objective function to be treated can be written as

$$J = |C| = \left| \int_{\Omega_0} \mathbf{S} \cdot (e^{T*} \mathbf{E}) \, d\Omega_0 \right|. \quad (12)$$

To simplify the study, a pair of rectangular electrodes is considered. Moreover, only one ‘parasitic’ mode is considered. So, the external excitation is applied along the  $\vec{Z}$ -axis. Thus, the modes to be controlled are those which correspond to motion along  $\vec{Z}$ . In addition, the material electromechanical coupling coefficient of quartz is very low, approximatively

(11)

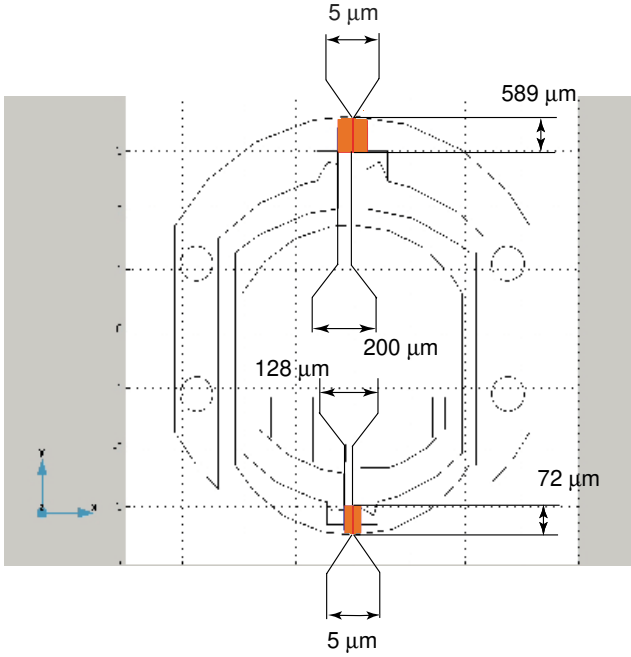
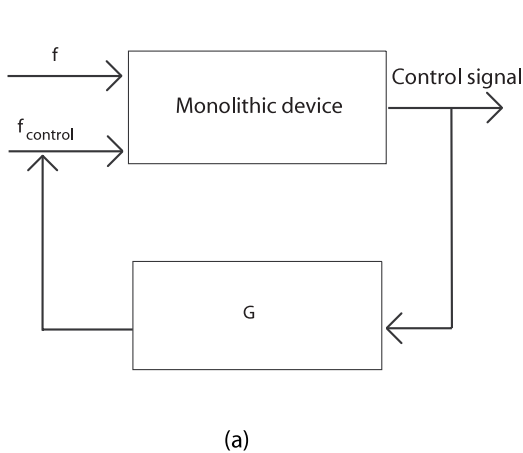


**Figure 9.** Location of rectangular actuating electrodes with their dimensions.

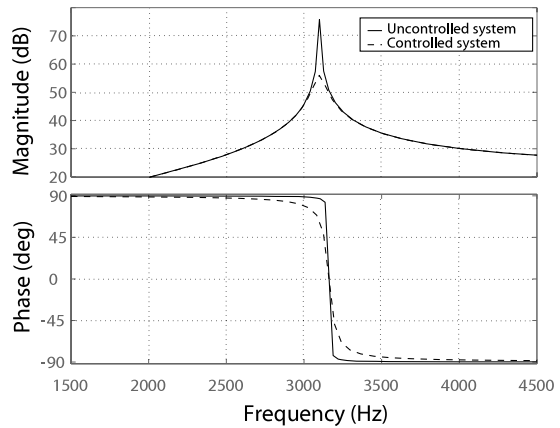
$10^{-2}$ . Consequently, the field of displacement and the electric field can be supposed to be perfectly uncoupled [40–44]. The study of these two fields is performed sequentially. As an aside and as shown in figure 7, electric field in a complex structure requires a 3D modeling. This is why, in this study, a 3D modeling of the device is used.

By considering  $E_2 = 0$  (rectangular electrodes) and a specific and confidential crystal cut, the criterion  $J$  can be rewritten as

$$J = \left| \int_{\Omega_0} (e_{11}^* E_1 S_1 + e_{12}^* E_1 S_2 + e_{13}^* E_1 S_3 + 2e_{14}^* E_1 S_4) d\Omega_0 \right|. \quad (13)$$



(a)



(b)

**Figure 10.** (a) Numerical control architecture. (b) Bode diagrams between external solicitation and velocity signal for uncontrolled system (solid line) and controlled system (dotted line).

## 5. Topological optimization of actuating electrodes

For the optimization process, a modal analysis and an electrostatic analysis are performed. This process leads to an optimal location of actuating electrodes on the device. Control of the ‘parasitic’ modes is carried out by this set of electrodes as so to induce feedback efforts.

### 5.1. Studied mesh case

The geometry of the device is meshed as depicted in figure 6. A finite-element formulation for the response of the piezoelectric solid is used [45]. The multiphysics equations (1)–(6) are discretized using a Lagrange-quadratic tetrahedral element that leads to a final discretized system of 65 103 degrees of freedom. Numerical integrations are performed using ten Gauss points per element.

### 5.2. Numerical optimization process

It is necessary to study and maximize the term (12). Initially, general strain evolution of the ‘parasitic’ natural mode of the structure is studied in order to locate areas of maximum strain. Thus, two areas of strong strains are delimited as shown in figure 8. An optimization process is performed for these two specific areas.

In postprocessing with Comsol<sup>®</sup> software, evolution of the various strains with respect to the coordinate along the  $\vec{Y}$ -axis for the studied mode is computed for Dirichlet electric conditions equal to zero ( $V_a = 0$ ). Strain evolutions are fitted by a polynomial approximation.

In addition, the analytical expression of the electric fields in electrostatics is determined by considering an electric field evanescent along the thickness axis [40]. Thus, evolution of the term (13) can be obtained for both studied areas. Actuating electrodes are optimized so as to obtain the term (13) as large as possible. The optimized rectangular actuating electrodes are located as depicted in figure 9.

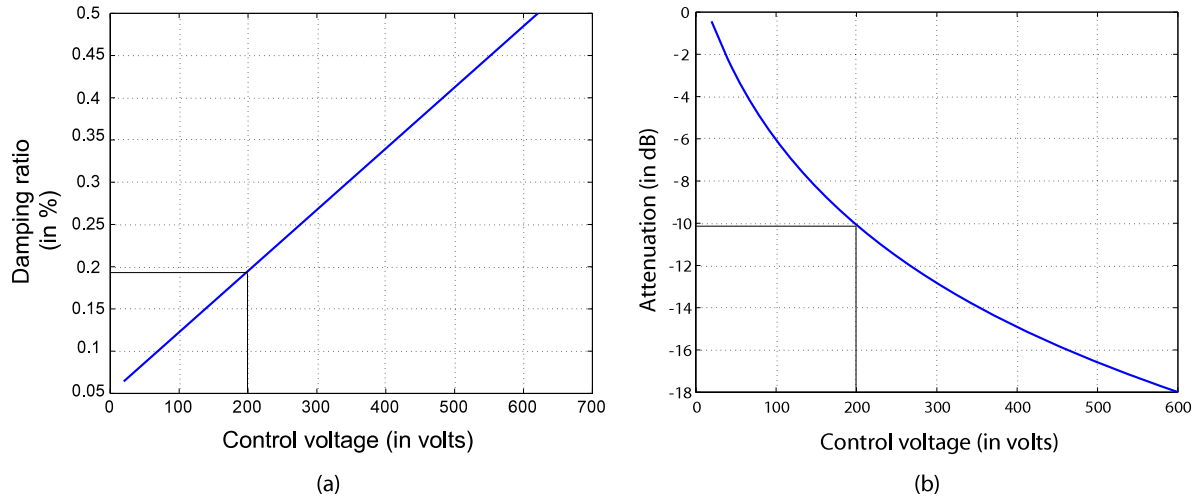


**Figure 11.** (a) Damping ratio evolution with respect to control voltage. (b) Resonance peak attenuation with respect to control voltage.

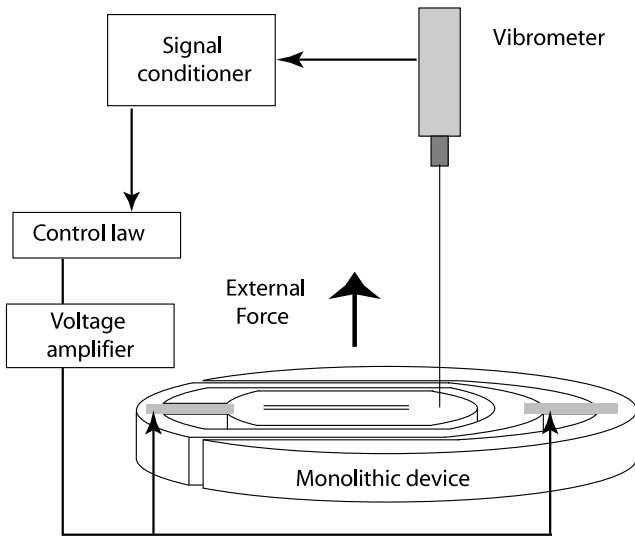


**Figure 12.** Experimental control scheme.

### 5.3. Active stabilization

The equations of motion are projected on the ‘parasitic’ natural mode. Thus, control study is reduced to a one-degree-of-freedom system. Consequently, it is obvious that it is just necessary to make a proportional feedback with an absolute velocity signal in order to increase the damping ratio of the device. This strategy is called direct velocity feedback (DVF) [46, 13].

The loop necessary for control is set up as shown in figure 10(a). The structure is perturbed by a random vibration of  $20g_{\text{rms}}$  amplitude and the performance results of the control feedback are observed.

The damping ratio evolution and resonance peak attenuation with respect to voltage applied to the optimized actuating electrodes are traced respectively in figures 11(a) and (b).

Considering the dimensions of the device, the voltage to be applied seems huge. But, quartz material is slightly piezoelectric [40–44], which explains this important value.

## 6. Experimental active stabilization

### 6.1. Experimental set-up

The control strategy is set up in order to stabilize the ‘parasitic’ modes by using an external measurement. A velocity measurement provided by a laser vibrometer from Ometron is chosen. The control electrodes that we used are deposited with the dimensions obtained during the optimization process.

A DVF control loop, that is to say a sky-hook strategy, is set up as illustrated in figure 12.

The studied accelerometer is clamped with a special support made of Nylon as shown in figure 13. A Siglab data acquisition system with four input channels and two output channels is employed for data acquisition and signal processing. The device is disturbed, along the  $\vec{Z}$ -axis, via a seismic table with a random vibration of  $20g_{\text{rms}}$  amplitude. The reference signal is the velocity that we measure with an Ometron vibrometer in a stationary coordinate system. The control law is a simple proportional feedback. This law is implemented with a DSpace<sup>®</sup> platform whose sampling frequency ( $f_{\text{sampling}} = 20\,000$  Hz) is much higher than frequency of the mode to be damped (around 3280 Hz). However, the control line limits the control voltage to 200 V. Thus, optimal control performances shown by the numerical study cannot be reached.

### 6.2. Experimental active stabilization with an external sensor

In figure 14, curves for uncontrolled (black line) and controlled (gray lines) systems are presented. These curves are a close-up of the mode studied for various control gains.

In table 1, the optimal results obtained during experiments are compared to simulated ones for the ‘parasitic’ mode. A maximal control voltage of about 200 V is reached.

A theoretical attenuation of  $-10$  dB, that is to say a damping ratio of 0.2%, is performed. During experiments, an attenuation of  $-13$  dB, that is to say a damping ratio of 0.19%, is obtained. The attenuation performance is a little different from simulation. This may be due to the initial damping

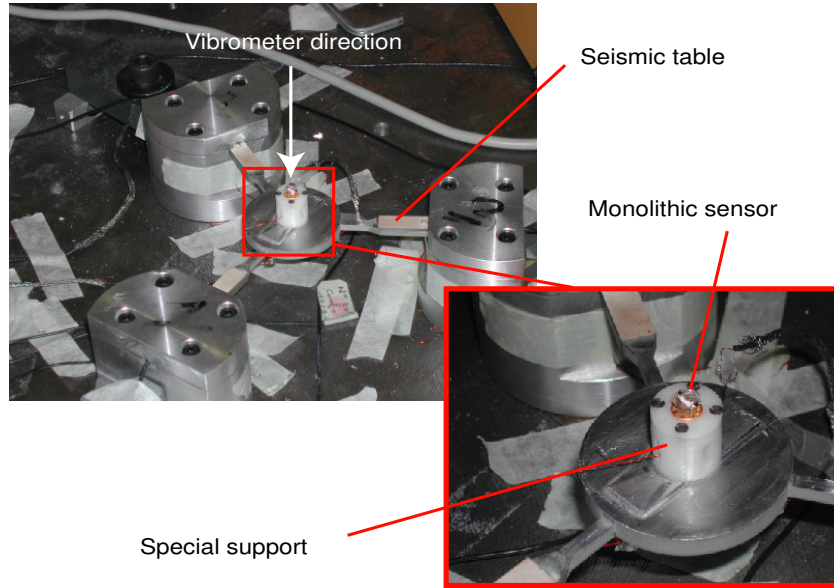


**Figure 13.** Experimental set-up.

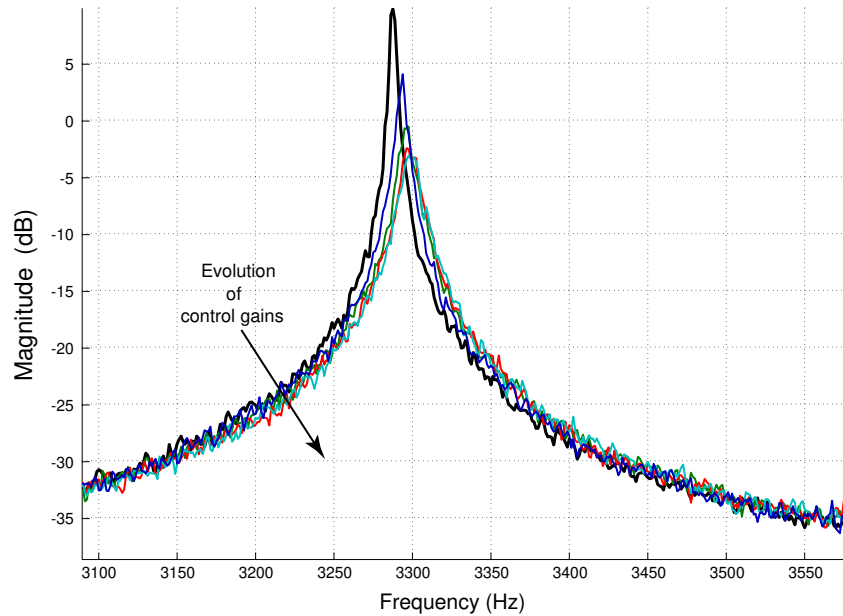


**Figure 14.** Bode diagrams between external excitation and velocity signal for different control gains between 0 and 2000.

**Table 1.** Comparison between numerical and experimental results for a 200 V control voltage.

	Numeric results	Experiment
Frequency	3180	3300
Attenuation	-10	-13
Damping ratio	0.2	0.19

introduced in modeling. The experimental damping ratio is hard to evaluate for this type of device. Nevertheless, the results listed in table 1 are in quite good correlation. Note that the ‘parasitic’ mode is damped in exploitable proportions so as to decrease its influence on device operation.

### 6.3. Experimental exploitations of the studied accelerometer

Currently, the commercial accelerometers are bonded and used on electronic cards. Their operation requires the use of instruments for signal processing and power supplies. Thus, control electronics necessary for vibration control (voltage amplifier, charge conditioning amplifiers, energy supply, devices for signal processing and real-time operation with a power supply) is already physically present on these electronic cards. To achieve vibration control, a reference signal is necessary. The first experiments, with the laser velocimeter used as a reference signal, demonstrate that optimized control electrodes can damp, in quite interesting proportions, the

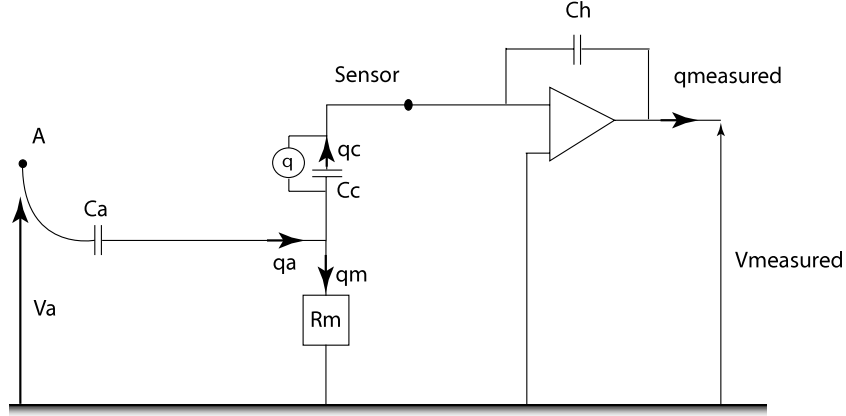


**Figure 15.** Equivalent electric scheme of the device connected to a conditioning amplifier.

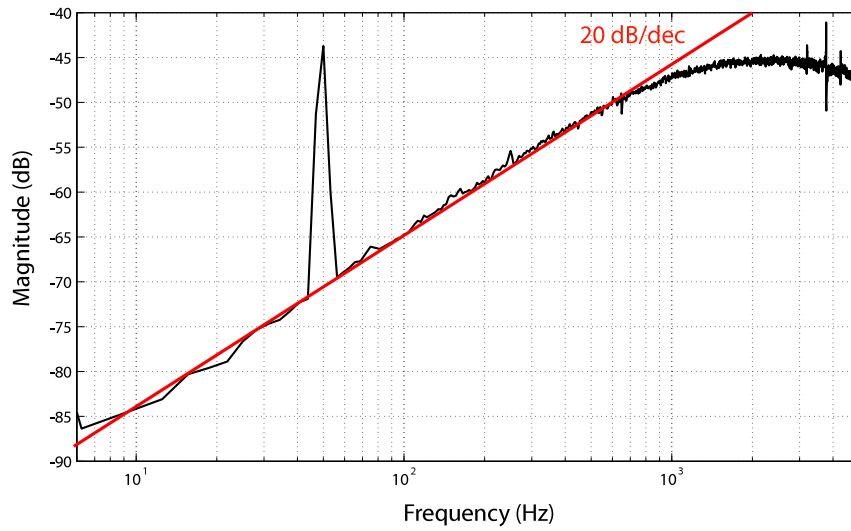


**Figure 16.** Bode diagrams between an input signal applied to electrodes of the sensitive central beam and an output signal issued to the actuating electrodes in a log scale.

‘parasitic’ eigenfrequencies. However, it is difficult to include physically in the device a laser velocimeter.

Consequently, for miniaturization, we try to use, as a reference signal for control, the signal provided by the sensor itself. The accelerometer signal is experimentally analyzed. The frequency response function (FRF) between an input signal applied to the electrodes of the sensitive central beam and an output signal issued to the optimized actuating electrodes is measured. The presence of a strong electric coupling is suspected. To evaluate this, the FRF is presented in a log-scale diagram. As shown in figure 16, a strong capacitive coupling exists between electrodes of the sensitive central beam (i.e. the sensor itself) and optimized control electrodes. Indeed, the 20 dB/dec slope in the magnitude diagram is a characteristic of a derivative function. This function is introduced into the system by a capacitive coupling between input and output [19]. The device connected to a conditioning amplifier can be electrically modeled as shown in figure 15. This device with respect to the sensing electrodes is equivalent to an electric capacitance and a generator of electric charges in parallel.

The relationship between control voltage and measurement can be written as

$$\frac{q_{\text{measured}}}{V_a} = \frac{C_h V_{\text{measured}}}{V_a} = \underbrace{\frac{C_a R_m C_c s}{1 + (R_m C_c + C_a R_m) s}}_A + \underbrace{\frac{(1 + C_a R_m s) H_{\text{sys}}}{1 + (R_m C_c + C_a R_m) s}}_B. \quad (14)$$

Part A is related to the contribution of the electric coupling and part B to the contribution of the mechanical system. Thus, the ‘parasitic’ natural modes are perfectly hidden by this coupling. Consequently, the signal issued to the sensor itself is not usable as an input of control strategy.

To overcome this difficulty, two solutions can be envisaged.

Observation electrodes, duly optimized, can be deposited on the device surface. This option requires a new design of the sensor to be controlled.

An active suspension system can be also added between the support on which the sensor is fixed (for example, an electronic card) and the sensor itself. This solution

makes it possible to withdraw the structure from its ambient environment in the frequency bandwidth which parasitizes operation of the structure [18–20]. This option does not require a new design of the sensor to be controlled and does not affect its operation.

## 7. Concluding remarks

A feasibility test of active stabilization of a monolithic vibrating beam sensor is performed. For a random excitation of  $20g_{\text{rms}}$  amplitude, it is necessary to apply, experimentally, to the actuating electrodes a voltage of approximately 200 V in order to obtain a damping ratio of 0.2%. This experimental implementation gives promising results with an external reference measurement. The trend and the performances of experimental control are in good correlation with modeling. But, the limitation of control voltage does not enable us to reach the breakdown limit and, consequently, the optimal control efficiency.

For miniaturization, using the signal provided by the sensor itself as the reference signal can be an interesting idea. Unfortunately, this signal is not usable as an input of the control strategy because of a strong capacitive coupling. To overcome this difficulty, two solutions can be envisaged. Observation electrodes, duly optimized, can be deposited onto the device, or an active suspension can be added between the support on which the sensor is fixed and the sensor itself.

## References

- [1] Gautschi G H 2002 *Piezoelectric Sensorics* (Berlin: Springer)
- [2] Benes E, Groschl M, Burger W and Schmid M 1995 Sensors based on piezoelectric resonators *Sensors Actuators A* **48** 1–21
- [3] Kusakabe H and Takigawa M 1992 Piezoelectric pressure sensor *US Patent Specification* 5142914
- [4] Dauwalter C R 1972 The temperature dependence of the force sensitivity of AT-cut quartz crystals *Proc. 26th Ann. Symp. Freq. Contr.* pp 108–12
- [5] EerNisse E P 1976 Calculations on the stress compensated (SC-Cut) quartz resonator *Proc. 30th Annual Symp. Freq. Contr.* pp 8–11
- [6] Ballato A 1977 Doubly rotated thickness mode plate vibrators *Phys. Acoust.* **13** 115–81
- [7] Vig J R and Mecker T R 1991 The aging of bulk acoustic wave resonators, filters and oscillators *Proc. 45th Annual Symp. Freq. Contr.* pp 77–101
- [8] Warner A W 1960 Design and performance of ultraprecise 2.5-mc quartz crystals units *Bell Syst. Tech. J.* **34** 1193–217
- [9] EerNisse E P, Ward R W and Wiggins R B 1988 Survey of quartz bulk resonator sensor technologies *IEEE Trans. Ultrason. Ferroelectr. Freq. Control* **35** 323–30
- [10] EerNisse E P and Wiggins R B 2001 Review of thickness-shear mode quartz resonator sensors for temperature and pressure *IEEE Sensors J.* **1** 79–87
- [11] Cooper M A and Singleton V T 2007 A survey of the 2001–2005 quartz crystal microbalance biosensor literature: application of acoustic physics to analysis of biomolecular interactions *J. Mol. Recognit.* **20** 154–84
- [12] Barbour N 2001 Inertial components—past, present and future *AIAA Guidance, Navigation and Control Conf. Exhibit (Montreal)*
- [13] Preumont A 2002 *Vibration Control of Active Structures: An Introduction* (Dordrecht: Kluwer–Academic)
- [14] Lagnese J E and Lions J-L 1988 *Modeling, Analysis and Control of Thin Plates* (Paris: Masson)
- [15] Chattopadhyay A, Seeley C E and Jha R 1999 Aeroelastic tailoring using piezoelectric actuation and hybrid optimization *Smart Mater. Struct.* **8** 83–91
- [16] Saravanan C, Ganesan N and Ramamurti V 2001 Semianalytical finite element analysis of active constrained layer damping in cylindrical shells of revolution *Comput. Struct.* **79** 1131–44
- [17] Pinto Correia I F, Mota Soares C M, Mota Soares C A and Herskovits J 2002 Active control of axisymmetric shells with piezoelectric layers: a mixed laminated theory with a high order displacement field *Comput. Struct.* **80** 2265–75
- [18] Meyer Y, Collet M and Delobelle P 2004 Active damping of electronic microcomponents with piezoelectric MEMS devices *Cansmart 04: Int. Workshop Smart Materials and Structures (Montréal)*
- [19] Meyer Y, Verdout T, Collet M, Baborowski J and Muralt P 2007 Active isolation of electronic micro components with piezoelectrically-transduced silicon MEMS devices *Smart Mater. Struct.* **16** 128–34
- [20] Meyer Y and Collet M 2007 Mixed control for robust vibration isolation: numerical energy comparison for an active micro suspension device *Smart Mater. Struct.* **16** 1361–9
- [21] Karnopp D C and Trikha A K 1969 Comparative study of optimization techniques for shock and vibration isolation *J. Eng. Ind.—Trans. ASME* **91** 1128–32
- [22] Preumont A, François A, Bossens F and Abu-Hanieh A 2002 Force feedback versus acceleration feedback in active vibration isolation *J. Sound Vib.* **257** 605–13
- [23] Ratajaski J M 1968 Force–frequency coefficient of singly-rotated vibrating quartz crystals *IBM J. Res. Dev.* **12** 92–9
- [24] EerNisse E P, Lukaszek T and Ballato A 1978 Variational calculation of force–frequency constants of doubly rotated quartz resonators *IEEE Trans. Son. Ultrason.* **25** 132–8
- [25] Danel J S and Delapierre G 1991 Quartz: a material for microdevices *J. Micromech. Microeng.* **1** 187–98
- [26] Bernstein J J and Weinberg M S 1994 Comb drive micromechanical tuning fork gyro *US Patent Specification* 5349855
- [27] Ljung B H G 2000 Coriolis gyro sensor *US Patent Specification* 6009751
- [28] Parent A, Masson S and Le Traon O 2005 Interest of high electromechanical coupling factor piezoelectric crystals in monolithic coriolis vibrating gyros (CVG) *Proc. EMSG Workshop (Les Vaux de Cernay)*
- [29] Paros J M, Busse D W, Chinn M D, Kistler W P and Weal R B 1988 Force-sensitive resonator load cell *US Patent Specification* 4751849
- [30] Chapman J E 2002 Vibrating beam force sensor having improved producibility *US Patent Specification* 6450032
- [31] Dulmet B 2005 Design of frequency-output resonant piezoelectric sensors *Proc. LFNM (Yalta, Crimea)* pp 184–8
- [32] Petrovich A, Weinberg M S and Williams J R 1994 Monolithic quartz resonator accelerometer *US Patent Specification* 5315874
- [33] Albert W C 1996 Monolithic quartz structure vibrating beam (VBA) prototype test results *Proc. IEEE Int. Freq. Cont. Symp. (Honolulu, HI)* pp 567–71
- [34] Le Traon O, Janiaud D, Muller S and Bouniol P 1998 The VIA vibrating beam accelerometer: concept and performance *Proc. IEEE Position Location and Navigation Symp. (Palm Springs, CA)*
- [35] Le Traon O, Janiaud D and Muller S 1999 Monolithic accelerometric transducer *US Patent Specification* 5962786
- [36] Le Traon O, Janiaud D, Lecorre B, Pernice M, Muller S and Tridera J-Y 2005 Monolithic differential vibrating beam accelerometer within an isolating system between the two resonators *Proc. 4th IEEE Sensors*

- [37] Bechman R 1958 Elastic and piezoelectric constants of alpha-quartz *Phys. Rev.* **110** 1060–1
- [38] Auld B A 1990 *Acoustic Fields and Waves in Solids* 2nd edn, vol 1–2 (Malabar, FL: Krieger)
- [39] Boyle W S and Kisliuk P 1955 Departure from Paschen's law of breakdown in gases *Phys. Rev.* **97** 255–9
- [40] Lewis J 1961 The effect of driving electrode shape on the electrical properties of piezo-electric crystals *Bell Syst. Tech. J.* **50** 1259–80
- [41] Sinha B K and Tiersten H F 1979 First derivatives of the fundamental elastic constants of quartz *J. Appl. Phys.* **50** 2732–9
- [42] Sinha B K 1987 A stress and temperature compensated orientation and propagation direction for surface acoustic wave devices *Proc. IEEE Trans. Ultrason. Ferroelectr. Freq. Control* **34** 64–74
- [43] Ballandras S and Bigler E 1992 Surface acoustic wave devices with low sensitivity to mechanical and thermoelastic stresses *J. Appl. Phys.* **72** 3272–81
- [44] Taziev R M 1994 Extreme pressure-sensitive cuts for surface acoustic waves in  $\alpha$ -quartz *Proc. Int. Freq. Contr. Symp.* pp 345–50
- [45] Naillon M, Coursant R H and Besnier F 1979 Analyse de structures pizoelectriques par une mthode d'elements finis *Acta Electron.* **25** 341–62
- [46] Balas M J 1979 Direct velocity feedback control of large space structures *J. Guid. Control Dyn.* **2** 252–3